Desalination and Water Treatment
www.deswater.com

doi: 10.5004/dwt.2023.29474

291 (2023) 117–130
April

Removal of uranium ions from aqueous solutions using nano-sized copper potassium hexacyanoferrate encapsulated O-carboxymethyl chitosan matrix by batch and fixed bed column methods

Huda Ammar[a], A.F. Shabaan[b], Salah M. El-Bahy[c,*], H.A. Elkhawaga[d], Amal M. Metwally[b]

[a]*Nuclear Materials Authority, El Maadi, Cairo, Egypt, email: ammar.huda@yahoo.com*
[b]*Chemistry Department, Faculty of Science, Benha University, Benha, Egypt, emails: afshaaban@hotmail.com (A.F. Shabaan), aml.metwaly@fsc.bu.edu.eg (A.M. Metwally)*
[c]*Department of Chemistry, Turabah University College, Taif University, P.O. Box: 11099, Taif 21944, Saudi Arabia, email: s.elbahy@tu.edu.sa*
[d]*Faculty of Engineering (Shoubra), Benha University, Shoubra, Egypt, email: Hanaa.elkhawaga@gmail.com*

Received 21 July 2022; Accepted 14 March 2023

ABSTRACT

The environment is at risk from radioactive waste containing uranium ions. A nano-sized copper potassium hexacyanoferrate encapsulated O-carboxymethylchitosan (CuHCF/O-CMCs) matrix was used to extract U(VI) ions from the manufactured wastewater in this investigation. The synthesized CuHCF/O-CMCs nanocomposite was prepared by methylation of chitosan to form O-carboxymethylchitosan (O-CMCs). The prepared nanoparticles of copper potassium hexacyanoferrate (CuHCF) were dispersed in the aqueous solution of O-CMCs in the presence of calcium chloride solution to give a CuHCF/O-CMCs nanocomposite. Fourier-transform infrared spectroscopy, scanning electron microscopy, energy-dispersive X-ray spectroscopy, transmission electron microscopy, X-ray diffraction, and thermal gravimetric analysis-differential scanning calorimetry confirmed the chemical structure of the synthesized CuHCF/O-CMCs composite. Effects of pH, concentration of U(VI), adsorption time, and temperature of solution on the uranium uptake using the batch method were investigated. The obtained results indicated that the highest value of removal capacity was 690 mg/g of U(VI) on the CuHCF/O-CMCs composite at pH 4, 1,000 mg/L U(VI), and 298 K. The isotherms, kinetic and thermodynamic parameters of the U(VI) adsorption were investigated. Moreover, the column method was studied for the U(VI) ions' removal by composite. The kinetics and interaction behavior of the removal process in continuous columns were described using theoretical models such as the Thomas model and the Yoon–Nelson model. The Thomas model and the Yoon–Nelson model were found to fit the experimental results well. The breakthrough data gave a good fit to the Thomas model. At a flow rate of 1 mL/min and a bed height of 2 cm, U(VI) had a maximum sorption capacity of 436.03 mg/g, corresponding to 57.11% uranium ion removal. The CuHCF/O-CMCs composite was eluted using 1 M HNO_3 and can be used repetitively five times with more than 93% of initial adsorption capacity.

Keywords: O-carboxymethylchitosan; Nanoparticles; Uranium ions; Batch technique; Column method

* Corresponding author.

1. Introduction

One naturally occurring element is uranium, found in soil, rocks, and aqueous sources. Uranium is produced by human activities such as uranium mining, nuclear power, phosphate fertilizers, and other industries [1,2]. Water containing radioactive pollutants such as uranium is the most harmful waste in the different wastewater industries. As a result, researchers are still looking into new methods for removing radioactive ions from liquid waste to dispose of them safely [3,4]. Uranium (U) is a poisonous and radioactive element used in various nuclear reactors. It has detrimental environmental impacts and should be eliminated from radioactive waste [5]. Eventually, uranium from nuclear industrial operations comes into touch with people after permeating the environment, contaminating water and soil, plants, and other living things. It causes serious diseases such as kidney damage and decreased liver functionality, followed by some diseases. One of the most dangerous diseases caused by exposure to uranium is the influence on children's bone development and DNA damage, leading to different cancer types due to uranium radioactivity [6–10]. Uranium is removed from aqueous solutions using a variety of techniques, such as chemical precipitation [11], solvent extraction and membrane separation [12], ion exchange and adsorption [13,14], electrocoagulation [15], and biological and passive treatment techniques [16,17]. However, all methods have their limitations when trying to find a method for selectively and economically separating and recovering the desired metal from side streams and effluents. Ion exchange and adsorption are the most common methods for removing uranium from industrial waste products and have been widely used [18]. Ion exchange is the most effective method of uranium removal since it can remove up to 98% of the uranium from wastewater [19]. The adsorbent is also a popular way to remove uranium because of its versatility and ease of use, as well as the fact that it can be reused and is not harmful to the body. Chitosan is a naturally occurring polymer with a high uptake for different metal ions. It can extract uranium from industrial wastewater with complex chemical compositions and is easily regenerated [20]. Metal ions and other pollutants are separated using chitosan and its derivatives [21–27]. Due to the simple preparation, low-cost, and high adsorption performance of hexacyanoferrates containing transition metals (MHCF) such as copper, iron, and zinc, they are used to remove metal ions from aqueous solutions [28]. But, some drawbacks are shown due to the small particle size of MHCF. Formation of the composite can overcome this drawback. The composite is prepared by encapsulating nanoparticle in polymer matrices [29,30]. Some of the prepared adsorbents include magnetic amidoxime beads [31], tetraethylenepentamine-modified magnetic chitosan resin [32], chitosan [1], and CuO/X-zeolite-based nanocomposites [33].

In this work, nanoparticles of CuHCF encapsulated in O-carboxychitosan (O-CMCs) are used to remove the uranium ions from aqueous solutions. Fourier-transform infrared spectroscopy (FT-IR), scanning electron microscopy (SEM), energy-dispersive X-ray spectroscopy (EDX), X-ray diffraction (XRD), and thermal gravimetric analysis-differential scanning calorimetry were studied for the CuHCF/O-CMCs composite. The adsorption mechanism may occur by exchanging the uranyl ions (UO_2^{2+}) with potassium ions (K^+) in the CuHCF in the composite and via complex chemical formation on the surface of the composite. The batch technique studied the adsorption of uranium onto CuHCF/O-CMCs composite. The relationship between the adsorption capacity and the aqueous solution's pH, initial concentration, shaking time, and solution temperature was investigated. Also, a variety of column experiments were conducted to figure out the breakthrough curves for various bed heights and flow rates.

2. Synthesis and characterization techniques

2.1. Materials

Chitosan with a 95.2% degree of deacetylation and polyvinyl alcohol (PVA) were purchased from Sigma-Aldrich, Germany. Copper sulfate ($CuSO_4{\cdot}5H_2O$), potassium hexacyanoferrate ($K_4[Fe(CN)_6]{\cdot}3H_2O$) were purchased from Sigma-Aldrich, Germany. U(VI) stock solution (1,000 mg/L) was prepared by dissolving 2.11 g of $UO_2(NO_3)_2{\cdot}6H_2O$ (Sigma-Aldrich, Germany) in 1.0 L of 0.05 M HNO_3. All other reagents were purchased from Aldrich and were of analytical grade.

2.2. Synthesis

2.2.1. Synthesis of O-CMCs

O-CMCs was synthesized according to Chen and Park's method [34]. Chitosan (13.5 g), sodium hydroxide (13.5 g), distilled water (25 mL), and isopropanol (100 mL) were all mixed in a 300 mL flask and allowed to swell and alkalize for an hour while being stirred magnetically at 30°C. The mixture was then dropped-wise with 15 g of monochloroacetic acid dissolved in 20 mL of isopropanol and reacted for 1 h at the same temperature. By adding 200 mL of 95% ethyl alcohol, the reaction was stopped. Filtration was used to collect the solid, which was then vacuum dried at 50°C. The powder was collected, and its composition was studied.

2.2.2. Synthesis of nanoparticles of CuHCF

In an aqueous medium, CuHCF powder was prepared by reacting a solution of ($CuSO_4{\cdot}5H_2O$) (10 wt.%) with a solution of ($K_4[Fe(CN)_6]{\cdot}3H_2O$) (10 wt.%) in the presence of PVA (6 wt.%) stabilizing agent. Drop by drop, ($CuSO_4{\cdot}5H_2O$) was added to ($K_4[Fe(CN)_6]{\cdot}3H_2O$) solution, stirring constantly. When the two solutions were mixed, a brown-colored CuHCF precipitate appeared. PVA and residual reactants were removed by ultracentrifugation and numerous washes with water. The precipitate was air-dried to obtain fine brown powder.

2.2.3. Synthesis of CuHCF/O-CMCs composite

We slowly added a solution of O-CMCs (2 g in 100 mL of distilled water) to a copper potassium hexacyanoferrate (3 g in 100 mL of distilled water) with stirring for 24 h. A solution of $CaCl_2$ (200 mL of 0.2 M) was dropped with slow stirring for 3 h. Afterward, the composite was removed from the solution and rinsed with water.

2.3. Characterization techniques

Vector 22 FT-IR Spectrometer, supplied by Bruker Corporation (Germany), was used to measure the FT-IR spectra of the synthesized compounds. The morphology of the prepared compounds was observed by scanning electron microscope-energy-dispersive X-ray spectroscopy (SEM-EDX), which was used to observe the surface morphology and particle size of the prepared CuHCF and the surface morphology of composite before and after adsorption of uranium ions. Micrographs were obtained using a (QUANTA 250 SEG, HOLANDA) microanalyzer microscope attached to EDX microanalysis system. Transmission electron microscopy (TEM) (JEOL [JEM-1230 Electron Microscopy]) was also used to determine the morphology and particle size of the sample. Thermal studies, including TGA were performed with SDT Q600 V20.5 Build 15 Thermogravimetric Analyzer. The test was performed in nitrogen atmosphere from room from 25 to 1,000°C at a heating rate of 10°C/min. The X-ray diffraction of CuHCF, O-CMCs, and CuHCF/O-CMCs composite was examined by Diano X-ray diffractometer using Cu Kα radiation (λ = 1.5418 Å).

2.4. Adsorption of uranium ions by batch method

The batch shaking technique was used to perform uranium sorption tests, which involved shaking 0.1 g of CuHCF/O-CMCs composite with 100 mL of aqueous uranium solution. Using a double-beam Jasco (UV-Visible) spectrophotometer (Japan), the residual content of uranium(VI) during equilibration was measured spectrophotometrically using Arsenazo III [35]. At a temperature of 298 K, the influence of pH in the range of 2–6 was investigated. At 298 K, the effect of the starting concentration was investigated using various U(VI) concentrations ranging from 100 to 1,200 mg/L. At different temperatures, the kinetics of the adsorption process were examined between 5 to 90 min. To check the repeatability of each result, all adsorption experiments were carried out three times.

2.5. Column technique

2.5.1. Uptake of U(VI) using column technique

Column adsorption tests were carried out in a CuHCF/O-CMCs composite-packed fixed-bed glass column with a length of 20 cm and an internal diameter of 1.2 cm. A pump was used to pump a solution of uranium ions at the optimum pH value and an initial concentration of 300 mg/L onto the column. Breakthrough investigations were carried out at 298 K, near room temperature. At various time intervals, the effluent at the column outlet was collected, and the remaining uranium (VI) concentration was determined, as indicated above. The experiment was stopped when the outlet uranium (VI) concentration equalled the intake uranium (VI) concentration. The effects of different factors, such as bed depth and flow rates, on column adsorption, were investigated.

2.6. Theory/calculation

2.6.1. Calculation of adsorption capacity

The following equation was used to estimate the uranium adsorption capacity q_e (mg/L) [36].

$$q = \frac{\left(C_0 - C_e\right)V}{W} \tag{1}$$

where V (L) is the volume of the aqueous solution, W (g) is the mass of the adsorbent material, C_0 (mg/L) is the initial uranium concentration, and C_e (mg/L) is the equilibrium uranium concentration.

2.6.2. Adsorption kinetic models

Three kinetic models, including the pseudo-first-order [Eq. (2)] [37], pseudo-second-order [Eq. (3)] [38], and intraparticle diffusion model [Eq. (4)] [39], were used to examine the kinetic process of U(VI) adsorption by CuHCF/O-CMCs.

$$\log\left(q - q_t\right) = \log q - \left(\frac{K_{\text{ads}}}{2.303}\right)t \tag{2}$$

$$\frac{t}{q_t} = \frac{1}{K_2 q^2} + \left(\frac{1}{q}\right)t \tag{3}$$

$$q_t = K_{\text{id}} t^{0.5} \tag{4}$$

where q (mg/g) represents the amount of U(VI) adsorbed at equilibrium, q_t (mg/g) represents the amount of U(VI) adsorbed at time t (min), K_{ads} (min^{-1}) represents the rate constant for a first-order kinetic model, K_2 (g/mg·min) represents a second-order kinetic model, and K_{id} (mg/g·min$^{0.5}$) represents an intraparticle diffusion model.

2.6.3. Adsorption isotherm models

Equilibrium adsorption isotherms are essential for providing the necessary data about the adsorption process' design. Three isotherm models, Langmuir [Eq. (5)] [40], Freundlich [Eq. (6)] [41], and Temkin [Eq. (7)] [42], can be used to investigate the distribution of U(VI) between the aqueous solution and the produced composite. The U(VI) affinity, surface characteristics, sorption capacity, and sorption mechanism may all be determined using these models.

$$\frac{C_e}{q} = \frac{C_e}{q_{\max}} + \frac{1}{K_L q_{\max}} \tag{5}$$

$$\log q = \frac{1}{n}\log C_e + \log K_F \tag{6}$$

$$q = B\ln K_T + B\ln C_e \tag{7}$$

where C_e (mg/L) is the equilibrium concentration of U(VI); q and $q_{\max}$ (mg/g) are the amounts of U(VI) sorbed at equilibrium and the maximum amount sorbed, respectively. The Langmuir affinity constant is K_L (L/mg); the Freundlich constants for adsorption capacity and heterogeneity factor are K_F (mg/g) and 1/n, respectively. The constants K_T (L/g) and B (J/mol) corresponding to equilibrium binding and heat of sorption, respectively.

Monolayer adsorption may be explained by the Langmuir isotherm model. The equilibrium parameter (R_L), which is determined by the equation below, can be used to represent the Langmuir isotherm.

$$R_L = \frac{1}{1 + K_L C_o} \tag{8}$$

The Langmuir constant is K_L (L/mg) and C_0 (mg/L) is defined as above. The R_L values suggest the shape of isotherm is linear (R_L = 1), unfavorable (R_L > 1), favorable (0 < R_L < 1) or irreversible (R_L = 0) [33,40].

The Freundlich adsorption model, on the other hand, was used to demonstrate heterogeneous adsorption. The Temkin isotherm model is another prominent model which is used in this work to fit the obtained results.

2.6.4. Thermodynamic parameters

Eqs. (9) and (10) can be used to calculate thermodynamic parameters such as Gibbs free energy $\Delta G°_{ads}$, change in enthalpy of adsorption $\Delta H°_{ads}$, and the change in entropy $\Delta S°_{ads}$.

$$\ln K_C = \frac{\Delta S^\circ_{ads}}{R} - \frac{\Delta H^\circ_{ads}}{RT} \tag{9}$$

$$\Delta G^\circ_{ads} = -RT \ln K_C \tag{10}$$

where T is the absolute temperature (K), K_C is the equilibrium constant (L/g), and R is the gas constant (8.314 J/mol·K). Eq. (11) provided K_C [36,43].

$$K_C = \frac{C_o - C_e}{C_e} \times \frac{V}{W} \tag{11}$$

where C_0 (mg/L) is the initial U(VI) concentration, C_e (mg/L) is the equilibrium U(VI) concentration (mg/L), V is the total volume of the solution in (L), and W is the weight of the dry composite in g.

2.6.5. Column data analysis

The U(VI) breakthrough curve was created by plotting C_{eff}/C_0 vs. time (t), with C_{eff} and C_0 representing effluent and influent U(VI) ion concentrations (mg/L), respectively. Eq. (12) gave the mass transfer zone (t) [44].

$$\Delta t = t_e - t_b \tag{12}$$

The bed exhaustion and breakthrough times are denoted by t_e and t_b, respectively.

Eq. (13) was used to compute the length of the mass transfer zone Z_m [45].

$$Z_m = Z\left(1 - \frac{t_b}{t_e}\right) \tag{13}$$

where Z is the bed height in cm.

The total column adsorption capacity (q_{total}) (mg) [46] was calculated from Eq. (14).

$$q_{total} = \frac{FA}{1{,}000} = \frac{F}{1{,}000} \int_{t=0}^{t=t_{total}} \left(C_{ads}\right) dt \tag{14}$$

The area under the breakthrough curve of the plot between C_{ads} (C_{ads} = C_0 – C_{eff}) as a function of time (t) is A (mg/min·L), the flow rate is F (mL/min), and the total flow time is t_{total} (min).

Eq. (15) calculated the equilibrium adsorption capacity ($q_{e(exp)}$) (mg/g) [41].

$$q_{e(exp)} = \frac{q_{total}}{m} \tag{15}$$

where m is the total dry weight of CuHCF/O-CMCs in grams.

Eq. (16) was used to calculate the total amount of U(VI) supplied to the column W_{total} (mg) [45].

$$W_{total} = \frac{C_o F t_{total}}{1{,}000} \tag{16}$$

The total removal percentage R (%).

$$R(\%) = \frac{q_{total}}{W_{total}} \times 100 \tag{17}$$

2.6.6. Column regeneration

After adsorption, the retained U(VI) is eluted with about 100 mL of 1 mol/L HNO_3 at a flow rate of 1 mL/min. After each cycle, the prepared adsorbent was washed with deionized water to prepare for the next adsorption cycle. The regenerated CuHCF/O-CMCs nanocomposite was reused in the next cycle of the adsorption experiments at an initial concentration of 300 mg/L, optimum pH, flow rate at 1.0 mL/min, and bed height of 2 cm. The experimental conditions were the same for all sorption–desorption processes. The regeneration process of U(VI) was conducted five times.

3. Result and discussion

3.1. Synthesis of CuHCF/O-CMCs composite

CuHCF/O-CMCs composite was prepared as shown in Fig. 1.

3.2. Characterization of CuHCF/O-CMCs composite

Fig. 2 shows FT-IR spectra of CuHCF, O-CMCs, and CuHCF/O-CMCs composite. The spectrum of CuHCF nanoparticles was shown in Fig. 2a, with a peak at 2,083 cm^{-1} due to the stretching vibration of the cyanide group (C≡N) and bands in the 470–585 cm^{-1} range due to (Fe–C) stretching [46]. Absorption peaks were found at 3,433 cm^{-1} (O–H stretch overlapped with N–H stretch), 2,993 cm^{-1} (C–H stretch), 1,635 cm^{-1} (C=O stretch of carboxyl methyl group

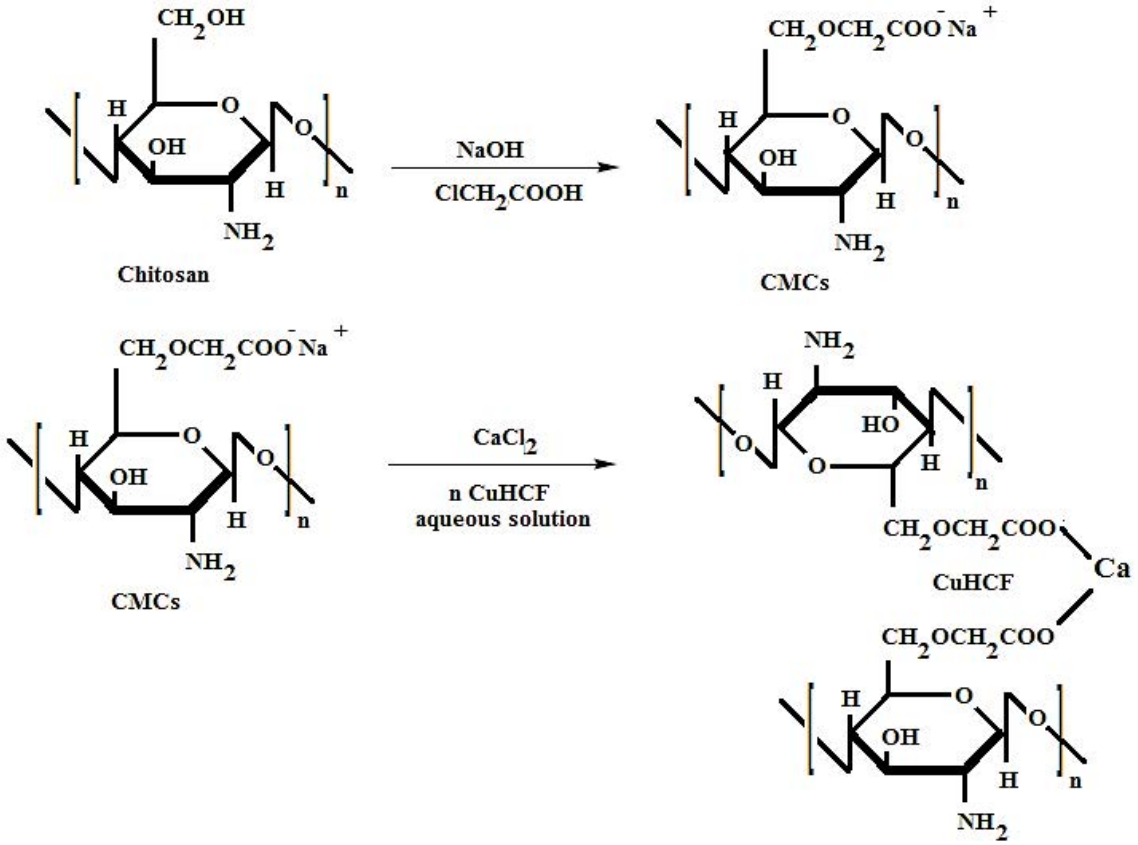

Fig. 1. Preparation of CuHCF/O-CMCs composite.

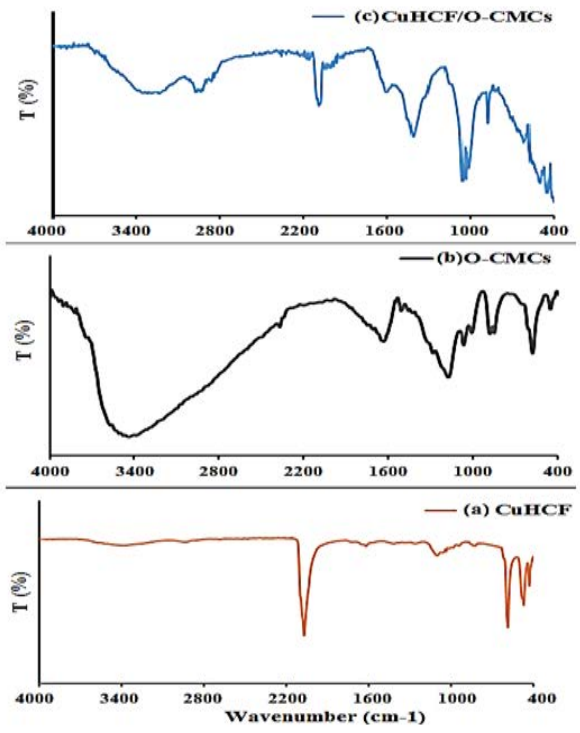

Fig. 2. FT-IR spectra of the synthesized (a) CuHCF, (b) O-CMCs and (c) CuHCF/O-CMCs composite.

overlapped with amide N–H bend) [47], 1,411 cm^{-1} (C–H bend), 1,327 cm^{-1} (C–N stretch), 1,172 cm^{-1} (bridge O stretch), and 1,064 cm^{-1} (C–O stretch) in Fig. 2b. The spectrum of the CuHCF/O-CMCs composite, shown in Fig. 2c, has a prominent peak at 2,083 cm^{-1}, which is attributable to the stretching vibration of the cyanide group (C≡N), as shown in Fig. 2a for CuHCF. The prominent peak in O-CMCs at 1,635 cm^{-1}, which corresponds to the C=O stretching of the carboxyl methyl group, was also visible in the CHCF/O-CMCs composite, Fig. 2c. The existence of these bands indicated that CuHCF had been encapsulated in O-CMCs.

SEM and TEM are good tools used to study the surface morphology of the synthesized products. As presented in Fig. 3a and b, the SEM and TEM of the prepared CuHCF nanoparticles exhibited a cubic structure with an average particle size between 50–100 nm. Fig. 4 shows SEM-EDX spectra of CuHCF/O-CMCs composite samples before and after uranium adsorption. The SEM images in Fig. 4 were studied to investigate the distribution of the CuHCF particles. The obtained images indicated that the CuHCF particles were uniformly distributed throughout the sample. After uranium adsorption, it was shown that uranium was uniformly adsorbed, and the electron-dense part (more bright), which is thought to be uranium adsorption, emerged after the adsorption of uranium ions Fig. 4b, as compared with Fig. 4a.

In EDX spectrum analysis, The uranium ion peaks appeared on the surface of the immobilized CuHCF/O-CMCs

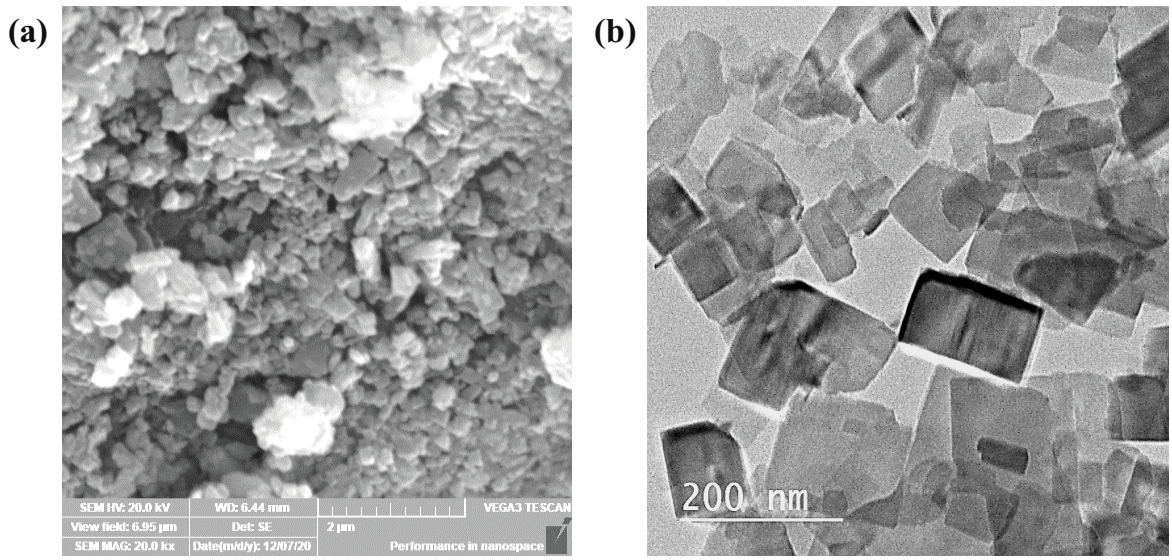

Fig. 3. (a) Scanning and (b) transmission electron microscopy of the prepared CuHCF nanoparticles.

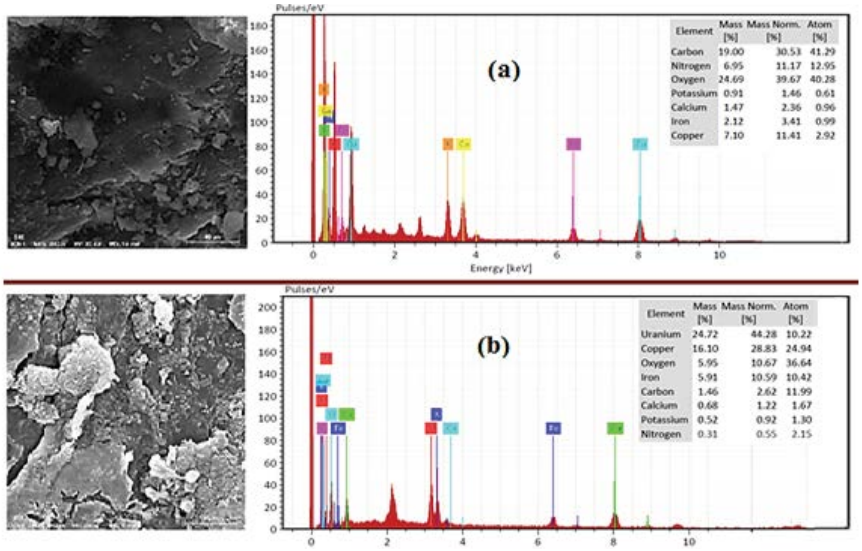

Fig. 4. Scanning electron microscopy-energy-dispersive X-ray spectroscopy spectra of CuHCF/O-CMCs composite samples (a) before and (b) after uranium adsorption.

composite. Additionally, the distribution of K^+ in CuHCF/O-CMCs before and after uranium uptake is indicated in Fig. 4, which confirmed that the concentration of K^+ slightly decreased after uranium uptake. Also, the elemental mapping before and after uranium removal was examined to monitor the distribution of uranium and K^+ before and after uptake of uranium (Fig. 5). The obtained data revealed homogeneous distribution of uranium ions with the decreased distribution of potassium ion attributable to the effectiveness of adsorption method.

Thermal analysis is a good tool for studying the prepared composite's thermal behavior and thermal stability. It can be seen in Fig. 6a that the degradation of O-CMCs proceeds in two steps: The first stage begins at roughly 77°C, and the second stage begins at around 255°C. The first stage is associated with water loss, as polysaccharides have a strong affinity for water and can thus be quickly hydrated. The second is due to the evaporation and removal of volatile products due to the thermal degradation of the main polysaccharides (containing saccharide rings and breakage of the C–O–C glycosidic bonds) [48]. Fig. 6b showed that the degradation steps of CuHCF/O-CMCs composite shifted to higher temperatures than O-CMCs. Which first step shifted to 90°C, while the second step shifted to 262°C; this proves that the presence of CuHCF in the polymer matrix affected thermal properties and increased the prepared composite's stability.

Fig. 7 shows the XRD patterns of (a) CuHCF and (b) CuHCF/O-CMCs composite. CuHCF nanoparticles have diffraction peaks in XRD pattern, which indicated the

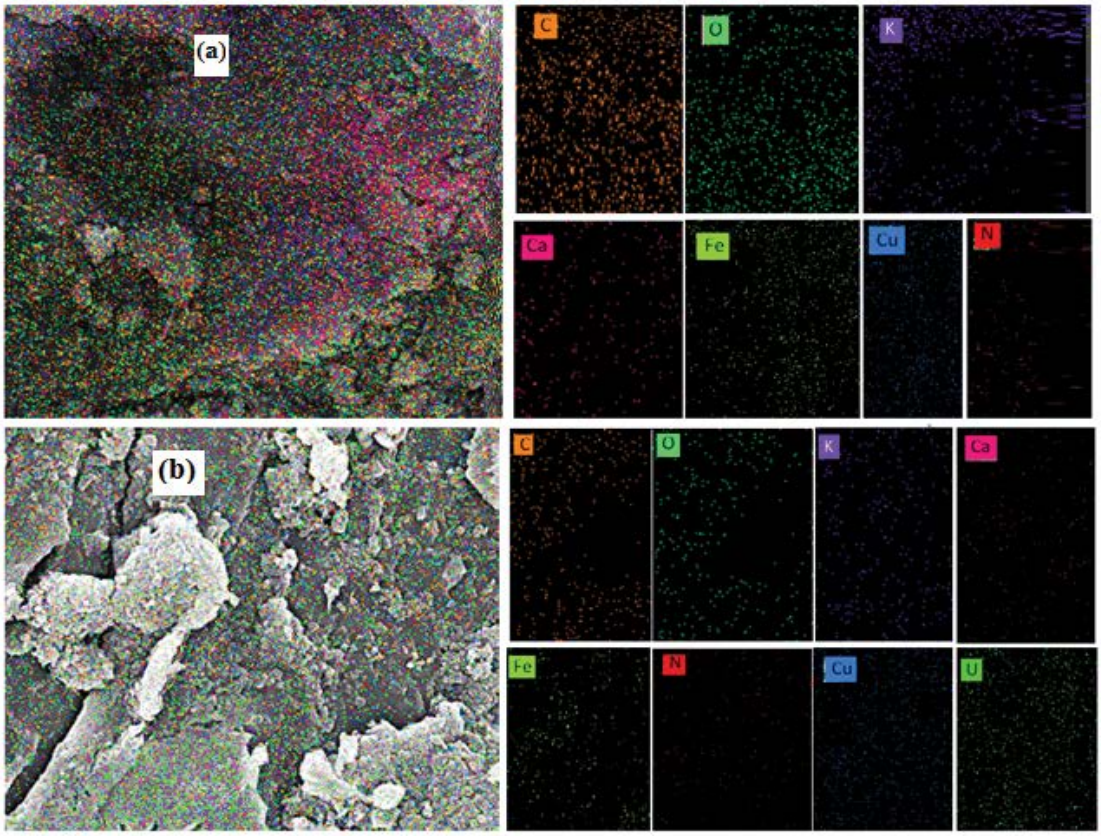

Fig. 5. Element mapping of CuHCF/O-CMCs composite samples (a) before and (b) after uranium adsorption.

crystalline nature of CuHCF nanoparticles (Fig. 7a). The pattern of CuHCF presented different peaks at 2θ values of 17.9°, 25°, 35.9°, 40.1°, 44.1°, and 51.1° which are due to Miller indexes of (200), (220), (400), (420), (424), and (440), respectively [49]. The crystalline structure of the synthesized CuHCF/O-CMCs composite was observed due to the diffraction peaks (Fig. 7b). This proves that CuHCF is incorporated into the binding matrix of O-CMCs.

3.3. Adsorption studied

3.3.1. Batch technique

3.3.1.1. Effect of pH

Experiments were conducted at pH ranging from 2 to 6 to investigate the effect of solution pH on uranium uptake by CuHCF/O-CMCs composite. The results are shown in Fig. 8. From the data, uranium's adsorption capacity increased as the pH increased from 2 to 4. The adsorption capacity reaches the maximum at pH 4. The adsorption capacity was reduced to 96.98 mg/g at pH 6. The reduced adsorption capacity at low acidic conditions is due to competition between H^+ and UO_2^{2+} ions for binding sites in the composite. Due to the deprotonation reaction [50–52], the composite surface became negatively charged. The electrostatic attraction between uranium species and the negative charge on the composite surface increased, increasing U(VI) adsorption capacity. Uranyl ions, such as UO_2^{2+} monomer, $[(UO_2)_2(OH)_2]^{2+}$ dimer, and $[(UO_2)_3(OH)_5]^+$ trimer, are all positively charged cationic species [47,48]. The deprotonated sites of the composite may retain uranium ions (UO_2^{2+}) via complex chemical compositions as well as ion exchange the uranyl (UO_2^{2+}) ions with potassium (K^+) in CuHCF in the composite. A pH of 4 was chosen as the optimum for the adsorption process.

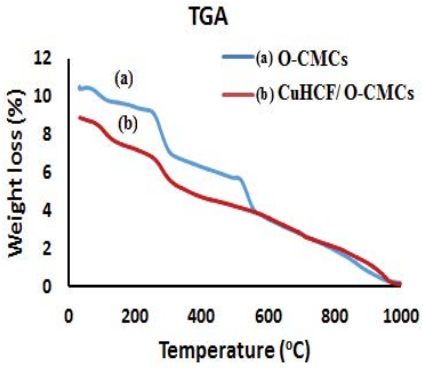

Fig. 6. Thermal gravimetric analysis for (a) synthesized O-CMCs and (b) CuHCF/O-CMCs.

3.3.1.2. Effect of contact time and adsorption dynamics

At temperatures ranging from 298 to 313 K, the influence of contact time on composite U(VI) adsorption capacity was

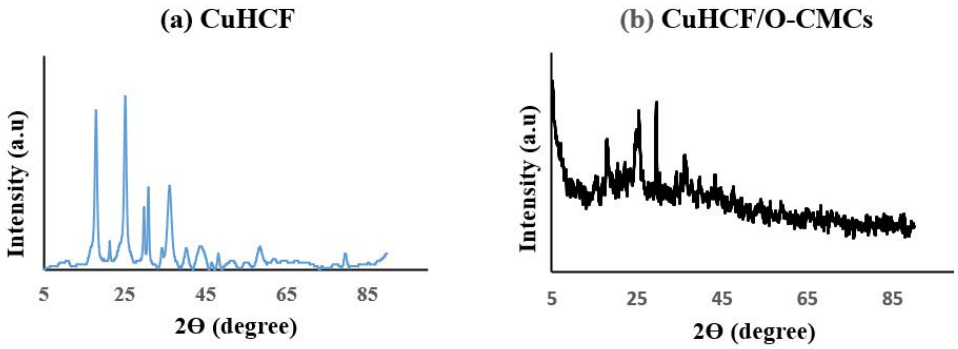

Fig. 7. X-ray diffraction pattern of (a) CuHCF and (b) CuHCF/O-CMCs composite.

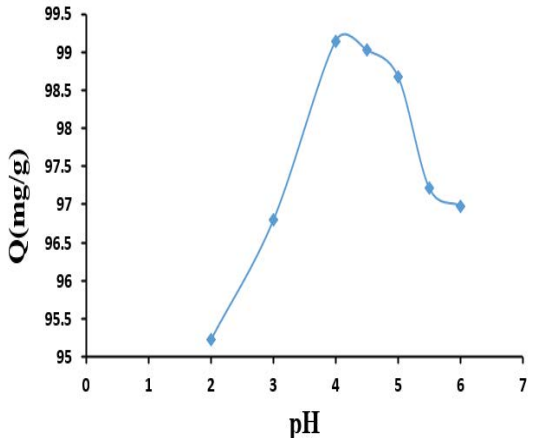

Fig. 8. Effect of solution pH on uranium uptake by CuHCF/O-CMCs composite.

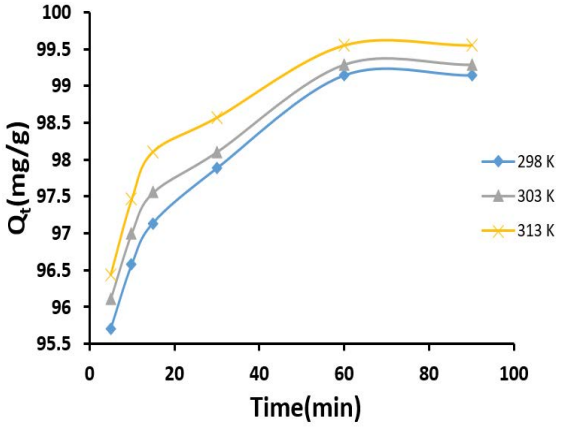

Fig. 9. Effect of contact time on uranium uptake by CuHCF/O-CMCs composite at different temperatures.

investigated. The data in Fig. 9 shows that the maximum U(VI) amount was adsorbed at 60 min for all three temperatures examined. At 298, 303, and 313 K, the maximum adsorption capacity (q_e) was 99.14, 99.29, and 99.55 mg/g, respectively. It shows that when the temperature increases, the adsorption capacity of U(VI) increases. It has a stronger driving force, which makes ion migration from the bulk solution to active site assembly easier. Adsorption kinetics is an important factor in adsorption efficiency. It can be used in adsorption research to estimate adsorption rates and provide important information for understanding the sorption process and reaction pathways. As a result, the data obtained were modeled using pseudo-first-order, pseudo-second-order, and intraparticle diffusion, as shown in Table 1. The high value of the linear correlation coefficient (R^2) of the pseudo-second-order kinetic model was equal to 1, which means that the pseudo-second-order kinetic model is more appropriate for describing U(VI) adsorption on composite.

3.3.1.3. Effect of initial U(VI) concentration and equilibrium isotherm model

U(VI) adsorption over CuHCF/O-CMCs composite using different initial concentrations of U(VI) from 100 to 1,200 mg/L at 298 K and pH = 4 were studied. Fig. 10. shows that U(VI) uptake increased with the increase of the initial concentration of U(VI).

Several isotherm models were chosen to fit the experimental results on uranium adsorption onto composite in this investigation. Langmuir, Freundlich, and Temkin models are the three most common. In Table 2, the three isotherm models are summarized. The Langmuir model had the highest linear correlation coefficient (R^2 = 0.9973), which fit the collected data better than other isotherm models. The obtained results indicated that the adsorption process fitted with the Langmuir model, which means that the adsorption of U(VI) occurs generally on a homogenous surface by the monolayer sorption process, with R_L values between 0.18 and 0.018 indicating that uranium adsorption is favorable at higher initial U(VI) concentration.

A comparison between the recent CuHCF/O-CMCs nanocomposite prepared in this work with those of different types of adsorbents for removal of U(VI) in newly published articles is tabulated in Table 3. Generally, the data listed in Table 3 shows that the synthesized CuHCF/O-CMCs nanocomposite has a good advantage in the uptake of U(VI) from wastewater more than the earlier published adsorbents.

3.3.1.4. Effect of temperature on the adsorption process

Adsorption experiments were conducted at different temperatures (298–313 K) to evaluate the influence of

temperature on adsorption, Fig. 11. The results showed that an increase in temperature favors the adsorption of uranium ions. The temperature dependence of uptake is associated with changes in various thermodynamic parameters, which are calculated and listed in Table 4. The ΔG°_{ads} value for U(VI) is negative, revealing that the U(VI) adsorption is spontaneous. The degree of spontaneity increased with increasing temperature, which suggests chemisorption rather than physisorption. [53]. The endothermic adsorption process, which increases the adsorption of U(VI) as temperature rises, is represented by the positive value of ΔH°_{ads} (VI). The positive value of ΔS°_{ads} could be clarified by the increased degree of randomness attributable to the liberation of water of hydration during the adsorption of U(VI)].

3.3.2. Fixed-bed column sorption

For U(VI) sorption onto CuHCF/O-CMCs composite at three constant influent flow rates (1, 3, and 5 mL/min) at 300 mg/L uranium ion concentrations, breakthrough curves (C_{eff}/C_0 vs. volume) were obtained at different bed depths (1, 2 cm) and three constant influent flow rates (1, 3, and 5 mL/min). The breakthrough curves are shown in Figs. 12 and 13. Eqs. (12)–(18) were used to compute the CuHCF/O-CMCs composite's sorption capacity (q_e) and removal percentage (R%) from the breakthrough curves, and the results are shown in Table 5.

3.3.2.1. Effect of flow rate

Figs. 12 and 13 show the breakthrough curves for U(VI) at various flow rates of 1, 2, and 3 mL/min through a column with a 1 and 2 cm bed height and an initial concentration of 300 mg/L of U(VI) solution and Table 5 displays the breakthrough factors. The findings demonstrate that the breakthrough curves shift towards a lower time scale and the breakthrough and exhaustion times shorten as the flow rate increases from 1 to 3 mL/min. This is due to the flow rate increasing, the amount of U(VI) removed in the column will be reduced because not all of the metal ions will have enough time to enter the CuHCF/O-CMCs composite pores from the solution. On the other hand, the percentage of U(VI) removal declined by 12% (Table 5) when the flow rate was increased by roughly three times, from 1 to 3 mL/min, as the metal ions would have left the column before the equilibrium occurred and the active life of the column was greatly decreased. The flow rate of 1 mL/min with the highest q_e was used for the following steps in this study because, as shown in Table 5, it is likely to be the critical flow rate. This suggests that the surface diffusion by the occupation

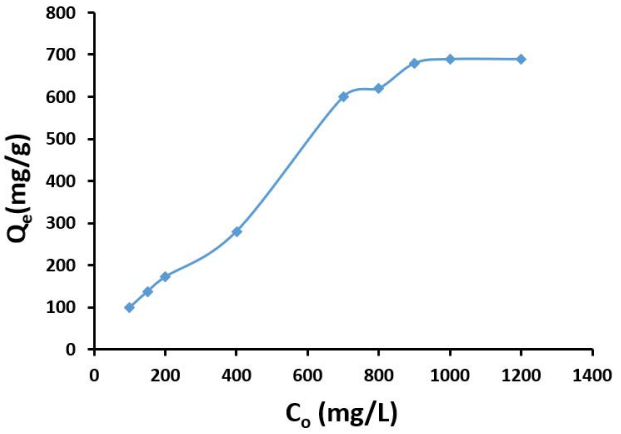

Fig. 10. Effect of the initial concentration of uranium on the adsorption process.

Table 1
Parameters of various kinetics models fitted to experimental data

Equations	Parameters	Temperature		
		298 K	303 K	313 K
Pseudo-first-order kinetic	q_e (mg/g)	33.41484	3.462532	3.350133
	K_{ads} (min^{-1})	0.035143	0.01629	0.018983
	R^2	0.9016	0.9397	0.9119
Pseudo-second-order kinetic	q_e (mg/g)	99.01	100	100
	K_2 (min^{-1})	0.031878	0.034483	0.04
	R^2	1	1	1
Intraparticle diffusion	K_{id}	0.4792	0.435	0.4069
	R^2	0.9356	0.9262	0.8869

Table 2
Parameters of Langmuir, Freundlich, and Temkin isotherms equation for adsorption of U(VI) on CuHCF/O-CMCs composite

Metal ion	Langmuir isotherm			Freundlich isotherm			Temkin isotherm		
	q_{max} (mg/g)	K_L (L/mg)	R^2	1/n	K_F	R^2	K_T	B	R^2
U(VI)	714	0.0445	0.9973	0.3575	90.40504	0.9567	1.01146	116.1	0.9245

of active sites on the surface of CuHCF/O-CMCs composite is the primary step at the overall U(VI) removal among the three steps of the uptake (film diffusion, pore diffusion, and surface diffusion) [54]. The MTZ length is remarkably stable under all studied flow rates at the same bed height (1 cm) and influent concentration (300 mg/L), which is most likely due to the same mechanism of t_e and t_b decreasing with increasing flow rate.

3.3.2.2. Effect of bed height

Fixed bed column studies were carried out using a column with CuHCF/O-CMCs composite at three constant flow rates of 1, 2, and 3 mL/min and an influent concentration of 300 mg/L of a single U(VI) metal ion for two different bed heights of 1 and 2 cm. Fig. 12, (1) display the breakthrough curves for the investigated ions at various bed heights, and Table 5 provides a summary of the breakthrough analysis. When adsorption was continued in any curve after the breakthrough point, the C_{eff}/C_0 would rise quickly to about 0.5 before descending more slowly to approach one and form S-shaped curves. When the bed height was increased from 1 to 2 cm, it was discovered that the breakthrough and exhaust times increased. This led to a higher removal percentage of U(VI) in the column because there were more binding sites available for sorption and because the transfer zone needs more time to reach to the column end so that the U(VI) ions can have more time to interact with CuHCF/O-CMCs composite. The MTZ length for the investigated metal roughly doubles when the bed height doubles at a constant flow rate and initial concentration. When the bed height increased twice (from 1 to 2 cm), the total metal removal percentage (R) increased by 18.59% for U(VI) because a larger volume of the metal solution could be treated and a higher percentage of metal removed in a bed with a higher length. In contrast, it is expected that, for various bed lengths, the composite's equilibrium adsorption capacity (q_e) will remain constant. The bed with 1 cm showed the highest equilibrium adsorption capacity compared to 2 cm, indicating that the adsorption capacity is still inversely proportional to bed height (Table 5). These findings are consistent with earlier findings [55–59]. CuHCF/O-CMC composite beads

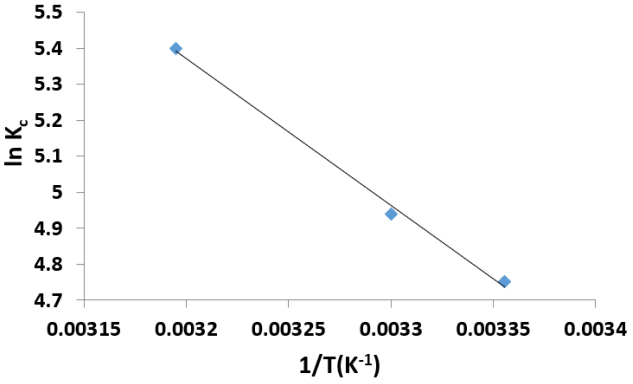

Fig. 11. Plot of $\ln K_C$ vs. $1/T$ for uranium adsorption into CuHCF/O-CMCs composite.

Table 3
Comparison of maximum adsorption capacity of (CuHCF/O-CMCs nanocomposite) among other adsorbents reported in the literature for the adsorption of U(VI)

Adsorbents	Adsorption capacity (mg/g)	pH	References
Nanoporous silica	29.40	4	[6]
Chitosan-tripolyphosphate (CTPP)	236.9	5	[7]
4-vinylpyridine-grafted-vinyltriethoxysilane-cellulose	134.00	7	[8]
Magnetic carboxymethyl chitosan nanoparticles functionalized with ethylenediamine	175.4	4.5	[9]
Tetraphenylimidodiphosphinate	99.89	4.5	[10]
Epichlorohydrin-activated magnetic chitosan microparticles (EPI-MG-CH)	357	5	[21]
Magnetic amidoxime functional chitosan (MAO-chitosan)	117.65	6	[22]
Phosphate- and amide-functionalized magnetic CS-carboxymethylcellulose composite (FCCP)	626	8	[22]
Humic acid modified magnetic chitosan nanoparticles (HA-MCNP)	47.9	5–7	[23]
Polyethylenimine-functionalized magnetic chitosan nanoparticles (MCN-PEI)	134.6	4	[24]
Si-6G PAMAM-PPAAM	434.78	4.5	[25]
CuHCF/O-CMCs nanocomposite	690	4	This work

Table 4
Thermodynamic parameters for U(VI) adsorption onto CuHCF/O-CMCs composite

Metal ion	$\Delta G°_{ads}$ (J/mol)			$\Delta H°_{ads}$ (kJ/mol)	$\Delta S°_{ads}$ (kJ/mol)	R^2
	298 K	303 K	313 K			
U(VI)	–169.773	–180.841	–202.979	489.9206	2.213736	0.9967

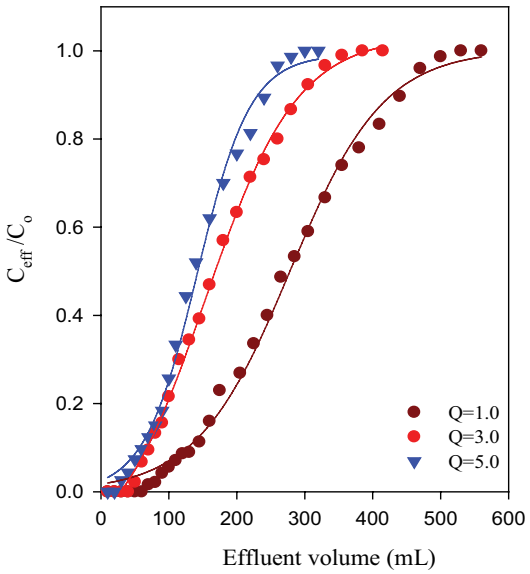

Fig. 12. Breakthrough curve for U(VI); initial concentration is 300 mg/L bed depth 1 cm at optimum pH and 298 K and flow rate (1, 3, and 5 mL/min).

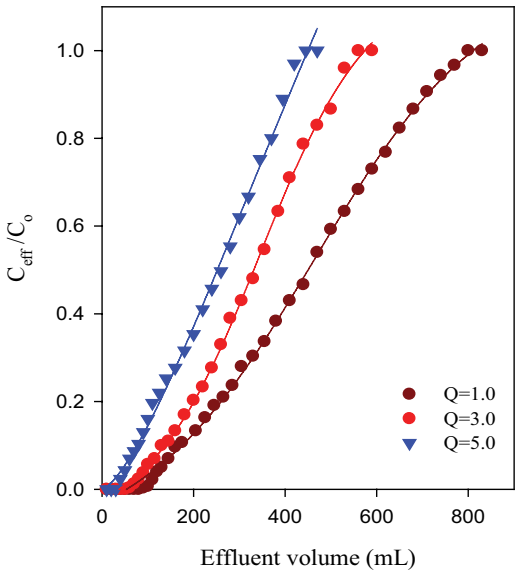

Fig. 13. Breakthrough curve for U(VI); initial concentration is 300 mg/L, bed depth is 2 cm at optimum pH and 298 K, and flow rate (1, 3, and 5 mL/min).

Table 5
Calculated column data parameters at different flow rates and different bed heights (C_0 = 300 mg/L)

Variables						Calculated parameters				
Metal ion	F (mL/min)	Z (cm)	t_b (min)	t_e (min)	Δt	W_{total} (mg)	q_{total} (mg)	q_e (mg/g)	R %	Z_m (cm)
U(VI)	1	1	70	530	460	168	80.90	539.35	48.16	0.868
	3	1	17	128	111	124.49	49.64	330.91	39.87	0.870
	5	1	6	60	54	96	40.69	271.29	42.39	0.9
	1	2	90	800	710	249	130.81	436.03	57.11	1.775
	3	2	20	187	167	177	94.78	315.94	53.55	1.786
	5	2	8	89	81	141	70.86	236.19	50.25	1.820

were found to have a sorption capacity for U(VI) of approximately 436.03 mg/g at a flow rate of 1 mL/min and a bed height of 2 cm in a fixed bed column.

3.3.2.3. Modeling of experimental column data

The application of the experimental data to various theoretical models in continuous adsorption, including the Thomas model and Yoon–Nelson model [59–63], was tested in order to examine the solute interaction behavior and estimate the breakthrough curves.

3.3.2.3.1. Thomas model

Column performance modeling frequently employs the Thomas model. Its derivation makes use of Langmuir adsorption–desorption kinetics and ignores axial dispersion. The Thomas model for the adsorption column is expressed as Eq. (18) [64]:

$$\frac{C_{eff}}{C_o}=\frac{1}{1+\exp\left[\frac{K_{Th}q_e m}{Q}-\frac{K_{Th}C_o V_{eff}}{Q}\right]} \tag{18}$$

where q_e (mg/g) is the expected adsorption capacity, m represents the weight of the sorbents (g), Q is the influent flow rate (mL/min), C_0 is the initial solution concentration (mg/L), and C_{eff} is the effluent solution concentration (mg/L). Eq. (19) represents the Thomas model's linear form.

$$\ln\left(\frac{C_o}{C_{eff}}-1\right)=\left[\frac{K_{Th}q_e m}{Q}-\frac{K_{Th}C_o V_{eff}}{Q}\right] \tag{19}$$

Experimental data were fitted into Eq. (19) to examine the Thomas model's kinetic coefficient (K_{Th}) and maximum uptake of the sorbent (q_e). Table 6 lists the results of linear regression and R^2 values, with values ranging from 0.9168 to 0.9807. The Thomas model's calculated q_e is higher than the experimental $q_{e'}$ as shown in Table 6. Table 6 also shows that the values of q_e and K_{Th} decreased as the adsorbent weight increased [65]. Thomas rate constant (K_{Th}) and bed length have been found to be inversely correlated; This explains why (K_{Th}) and (q_e) values decreased as well as a decrease in the transport rate of U(VI) from the aqueous solution to the composite. Due to the lack of available reaction sites,

Table 6
Thomas and Yoon–Nelson models constants at different flow rates and different bed heights (C_o = 300 mg/L)

Variables			Thomas model			Yoon–Nelson model			
Metal ion	F (mL/min)	Z (cm)	q_e (mg/g)	K_{Th} (L/mg·min)	R^2	K_{YN} (min^{-1})	τ (min)	R^2	$\tau_{exp.}$ (min)
U(VI)	1	1	558.68	5.43×10^{-5}	0.976	0.0163	279.34	0.976	270.75
	3	1	350.32	0.000218	0.966	0.0654	58.39	0.966	55.37
	5	1	289.68	0.00046	0.981	0.1380	28.97	0.981	27.22
	1	2	453.96	3.23×10^{-5}	0.917	0.0097	453.96	0.917	453.64
	3	2	329.99	0.000138	0.934	0.0414	107.62	0.934	112.51
	5	2	243.50	0.00023333	0.948	0.0700	48.70	0.948	52.24

the value of q_e decreased as the flow rate increased, but the value of K_{Th} increased; the Thomas rate constant for U(VI) would be increased by the shorter bed and higher flow rate. As can be seen, the experimental results support the theoretical findings.

3.3.2.3.2. Yoon–Nelson model

This model is simpler than other models and requires no data about the system's characteristics, such as the adsorbent type and the adsorption bed's physical properties. Eq. (20) represents the Yoon–Nelson equation [66]:

$$\frac{C_{eff}}{C_o - C_{eff}} = \exp\left(K_{YN}\frac{V_{eff}}{Q} - \tau K_{YN}\right) \tag{20}$$

where τ (min) is the of time needed for 50% of the adsorbate to breakthrough and K_{YN} (min^{-1}) is the rate constant. Eq. (21) represents the Yoon–Nelson model's linear form.

$$\ln\left(\frac{C_{eff}}{C_o - C_{eff}}\right) = \frac{K_{YN}}{Q}V_{eff} - \tau K_{YN} \tag{21}$$

Linear regression results and values of R^2 are presented in Table 6. With increasing adsorbent dose, it was found that the rate constant (K_{YN}) decreased and the time needed for 50% adsorbate breakthrough (τ) increased. Additionally, it was discovered that the rate constant (K_{YN}) rises in proportion to the rise in flow rate. The time needed for 50% adsorbate breakthrough (τ) decreased with increasing flow rate because metal ions had a shorter residence time in the adsorbent bed (Table 6). The experimental data and model match well, as can be seen. It can be said that the Yoon–Nelson and Thomas models are both suitable to describe fixed-bed operations.

3.3.3. Desorption

The regeneration of the loaded CuHCF/O-CMCs nanocomposite by U(VI) was achieved using 1 M HNO_3 at 298 K. The reusability of CuHCF/O-CMCs nanocomposite was checked by five successive adsorption–desorption cycles according to the following equation [22]:

$$\text{Regeneration efficiency \%} = \frac{\text{Uptake of metal ion in the second cycle}}{\text{Uptake of metal ion in the first cycle}} \times 100 \tag{22}$$

From the uptake–elution process, it is clear that the adsorption capacity of the newly prepared CuHCF/O-CMCs nanocomposite was hardly affected even after repeated five regeneration cycles. Over five cycles, the adsorption capacity decreased from 100% to 99%, 98%, 97%, 95%, and 93%, respectively.

4. Conclusion

An easy method to prepare a new adsorbent based on CuHCF nanoparticles encapsulated in O-CMCs was investigated. Characterization of the composite was studied using FT-IR, SEM, EDX, XRD and TGA. Using batch and column techniques, the prepared composite's ability to adsorb uranium was investigated. The influence of important factors such as pH, U(VI) concentration, shaking time, and solution temperature were examined. The obtained results showed that the highest value of adsorption capacity was 690 mg/g of U(VI) on CuHCF/O-CMCs composite at pH 4, 1,000 mg/L U(VI), and 298 K. The adsorption isotherms and kinetic and thermodynamic parameters of the U(VI) adsorption process were studied. The obtained results indicated that the adsorption process fitted with the Langmuir model, which means that the removal of U(VI) occurs generally on the homogenous surface. Pseudo-second-order kinetic model is more suitable for illustrating the adsorption of U(VI) on composite. Also, the column method was studied for the U(VI) ions removal by composite. Theoretical models such as the Thomas and Yoon–Nelson models were used to describe adsorption's kinetics and interaction behavior in a continuous column. Experimental data were compared to the kinetic models of Thomas and Yoon–Nelson. For U(VI) adsorption under various operating conditions, linear regression analysis was used to determine the model's parameters. The experimental results matched the models of Thomas and Yoon–Nelson well. The Thomas model was able to reasonably predict the experimental column results for the fixed-bed column system in this study. A maximum uptake of 453.96 mg/g was found for U(VI) at a flow rate of 1 mL/min and a bed height of 2 cm, corresponding to 57.11% of metallic ion

removal. Elution of U(VI) using the column technique was successfully performed using 1 M $HNO_{3,}$ and the CuHCF/O-CMCs composite could be applied repeatedly five times with little reduction (≈1%–7%) in the uptake of U(VI).

Acknowledgement

The researchers would like to acknowledge Deanship of Scientific Research, Taif University for funding this work.

References

[1] M. Szlachta, R. Neitola, S. Peräniemi, J. Vepsäläinen, Effective separation of uranium from mine process effluents using chitosan as a recyclable natural adsorbent, Sep. Purif. Technol., 253 (2020) 117493, doi: 10.1016/j.seppur.2020.117493.
[2] T.M. Kayzar, A.C. Villa, M.L. Lobaugh, A.M. Gaffney, R.W. Williams, Investigating uranium distribution in surface sediments and waters: a case study of contamination from the Juniper Uranium Mine, Stanislaus National Forest, CA, J. Environ. Radioact., 136 (2014) 85–97.
[3] D.A. Fungaro, M. Yamaura, R.G. Craesmeyer, Uranium removal from aqueous solution by zeolite from fly ash-iron oxide magnetic nanocomposite, Int. Rev. Chem. Eng., 4 (2012) 353–258.
[4] D. Goswami, A.K. Das, Preconcentration and recovery of uranium and thorium from Indian monazite sand by using a modified fly ash bed, J. Radioanal. Nucl. Chem., 258 (2003) 249–254.
[5] M.A. Mahmoud, Removal of uranium(VI) from aqueous solution using low cost and eco-friendly adsorbents, J. Chem. Eng. Process Technol., 4 (2013) 169, doi: 10.4172/2157-7048.1000169.
[6] M.K. Sureshkumar, D. Das, M.B. Mallia, P.C. Gupta, Adsorption of uranium from aqueous solution using chitosan-tripolyphosphate (CTPP) beads, J. Hazard. Mater., 184 (2010) 65–72.
[7] Y. Jung, S. Kim, S.J. Park, J.M. Kim, Application of polymer modified nanoporous silica to adsorbents of uranyl ions, Colloids Surf., A, 313–314 (2008) 162–166.
[8] T.S. Anirudhan, J. Nima, P.L. Divya, Adsorption and separation behaviour of uranium(VI) by 4-vinylpyridine-grafted-vinyltriethoxysilane-cellulose ion imprinted polymer, J. Environ. Chem. Eng., 3 (2015) 1267–1276.
[9] L. Zhou, H. Zou, Y. Wang, Z. Huang, Y. Wang, T. Luo, Z. Liu, Adesoji, A. Adesina, Adsorption of uranium(VI) from aqueous solution using magnetic carboxymethyl chitosan nano-particles functionalized with ethylenediamine, J. Radioanal. Nucl. Chem., 308 (2016) 935–946.
[10] J. Tan, Y. Wang, N. Liu, M. Liu, Adsorption of uranium(VI) from aqueous solution by tetraphenylimidodiphosphinate, J. Radioanal. Nucl. Chem., 315 (2018) 119–126.
[11] M.F. Hamza, I.E. El-Aassy, E. Guibal, Integrated treatment of tailing material for the selective recovery of uranium, rare earth elements and heavy metals, Miner. Eng., 133 (2019) 138–148.
[12] R. Chiarizia, E.F. Horwitz, Study of uranium removal from groundwater by supported liquid membranes, Solvent Extr. Ion Exch., 8 (1990) 65–98.
[13] E. Rosenberg, G. Pinson, R. Tsosie, H. Tutu, E. Cukrowska, Uranium remediation by ion exchange and sorption methods: a critical review, Johnson Matthey Technol. Rev., 60 (2016) 59–77.
[14] C. Zhao, J. Liu, Y. Deng, Y. Tian, G. Zhang, J. Liao, J. Yang, Y. Yang, N. Liu, Q. Sun, Uranium(VI) adsorption from aqueous solutions by microorganism-graphene oxide composites via an immobilization approach, J. Cleaner Prod., 236 (2019) 117624, doi: 10.1016/j.jclepro.2019.117624.
[15] E. Nariyan, M. Sillanpää, C. Wolkersdorfer, Uranium removal from Pyhäsalmi/Finland mine water by batch electrocoagulation and optimization with the response surface methodology, Sep. Purif. Technol., 193 (2018) 386–397.
[16] M. Kalin, G. Kießig, A. Küchler, Ecological water treatment processes for underground uranium mine water: progress after three years of operating a constructed wetland, Uranium Aquat. Environ., 236 (2002) 587–596.
[17] J. Li, Y. Zhang, Remediation technology for the uranium contaminated environment: a review, Procedia Environ. Sci., 13 (2012) 1609–1615.
[18] A. Rahmati, A. Ghaemi, M. Samadfam, Kinetic and thermodynamic studies of uranium(VI) adsorption using Amberlite IRA-910 resin, Ann. Nucl. Energy, 39 (2012) 42–48.
[19] L.M. Camachoa, S. Deng, R.R. Parra, Uranium removal from groundwater by natural clinoptilolite zeolite: effects of pH and initial feed concentration, J. Hazard. Mater., 175 (2010) 393–398.
[20] R.A.A. Muzzarelli, Potential of chitin/chitosan-bearing materials for uranium recovery: an interdisciplinary review, Carbohydr. Polym., 84 (2011) 54–63.
[21] M.F. Hamza, J.-C. Roux, E. Guibal, Uranium and europium sorption on amidoxime-functionalized magnetic chitosan microparticles, Chem. Eng. J., 344 (2018) 124–137.
[22] S. Zhuang, R. Cheng, M. Kang, J. Wang, Kinetic and equilibrium of U(VI) adsorption onto magnetic amidoxime-functionalized chitosan beads, J. Cleaner Prod., 188 (2018) 655–661.
[23] X. Guo, R. Chen, O. Liu, J. Liu, H. Zhang, J. Yu, R. Li, M. Zhang, J. Wang, Superhydrophilic phosphate and amidefunctionalized magnetic adsorbent: a new combination of anti-biofouling and uranium extraction from seawater, Environ. Sci. Nano, 5 (2018) 2346–2356.
[24] H. Basu, S. Saha, M.V. Pimple, R.K. Singhal, Novel hybrid material humic acid impregnated magnetic chitosan nano particles for decontamination of uranium from aquatic environment, J. Environ. Chem. Eng., 7 (2019) 103–110
[25] G. Sun, L. Zhou, X. Tang, Z. Le, Z. Liu, G. Huang, *In situ* formed magnetic chitosan nanoparticles functionalized with polyethylenimine for effective U(VI) sorption, J. Radioanal. Nucl. Chem., 325 (2020) 595–604.
[26] H. Ammar, A.F. Shaaban, T.A. Lasheen, E.A. Nouh, Preparation of new modified silica gel terminated with phenylphosphonic acid-amide moieties for adsorption of uranium(VI) from aqueous solutions, J. Radioanal. Nucl. Chem., 331 (2022) 3657–3670.
[27] E. Guibal, Interactions of metal ions with chitosan-based sorbents: a review, Sep. Purif. Technol., 38 (2004) 43–74.
[28] C. Loos-Neskovic, S. Ayrault, V. Badillo, B. Jimenez, E. Garnier, M. Fedoroff, Structure of copper-potassium hexacyanoferrate(II) and sorption mechanisms of cesium, J. Solid State Chem., 177 (2004) 1817–1828.
[29] Y.K. Kim, Y. Kim, S. Kim, D. Harbottle, J.W. Lee, Solvent-assisted synthesis of potassium copper hexacyanoferrate embedded 3D-interconnected porous hydrogel for highly selective and rapid cesium ion removal, J. Environ. Chem. Eng., 5 (2017) 975–986.
[30] I. Lee, C.W. Park, S.S. Yoon, H.-M. Yang, Facile synthesis of copper ferrocyanide-embedded magnetic hydrogel beads for the enhanced removal of cesium from water, Chemosphere, 224 (2019) 776–785.
[31] Y. Zhao, J. Li, L. Zhao, S. Zhang, Y. Huang, X. Wu, X. Wang, Synthesis of amidoxime-functionalized Fe_3O_4@SiO_2 core–shell magnetic microspheres for highly efficient sorption of U(VI), Chem. Eng. J., 235 (2014) 275–283.
[32] K.Z. Elwakeel, A.A. Atia, E. Guibal, Fast removal of uranium from aqueous solutions using tetraethylenepentamine modified magnetic chitosan resin, Bioresour. Technol., 160 (2014) 107–114.
[33] M.R. Abdi, H.R. Shakur, K.R.E. Saraee, M. Sadeghi, Effective removal of uranium ions from drinking water using CuO/X zeolite based nanocomposites: effects of nano concentration and cation exchange, J. Radioanal. Nucl. Chem., 300 (2014) 1217–1225.
[34] X.G. Chen, H.J. Park, Chemical characteristics of O-carboxymethyl chitosans related to the preparation conditions, Carbohydr. Polym., 53 (2003) 355–359.
[35] Z. Marczenko, Separation and Spectrophotometric Determination of Elements, Ellis Harwood, Chichester, 1986.

[36] S.M. El-Bahy, Z.M. El-Bahy, Immobilization of 2-amino pyridine onto poly(acrylonitrile-co-N,Ń-methylenebisacrylamide) nanoparticles for the removal of Hg(II), Cd(II) and Cr(III): batch and column techniques, J. Environ. Chem. Eng., 5 (2017) 3560–3571.
[37] S. Lagergren, Zur theorie der sogenannten adsorption geloster stoffe, Kungliga Svenska Vetenskapsakademiens, Handlingar, 24 (1898) 1–39.
[38] Y.S. Ho, Second-order kinetic model for the sorption of cadmium on to tree fern: a comparison of linear and non-linear methods, Water Res., 40 (2006) 119–125.
[39] W.J. Weber, J.C. Morris, Equilibria and capacities for adsorption on carbon, J. Sanit. Eng. Div., 90 (1964) 79–91.
[40] I. Langmuir, The adsorption of gases on plane surfaces of glass, mica and platinum, J. Am. Chem. Soc., 40 (1918) 1361–1403.
[41] H. Freundlich, Adsorption in solution, Phys. Chem. Soc., 40 (1906) 1361–1368.
[42] M.J. Temkin, V. Phyzev, Recent modifications to Langmuir isotherms, Acta Physiochim. USSR, 12 (1940) 217–222.
[43] S.M. El-Bahy, D.A. Fadel, Z.M. El-Bahy, A.M. Metwally, Rapid and highly efficient cesium removal by newly synthesized carbomer encapsulated potassium copper hexacyanoferrate composite, J. Environ. Chem. Eng., 6 (2018) 1875–1885.
[44] S.M. El-Bahy, New iminodiacetate chelating resin-functionalized Fe_3O_4 nanoparticles: synthesis, characterization, and application for the removal of some noxious metal ions from wastewater, J. Chem. Eng. Data, 63 (2018) 2299–2313.
[45] H. Yang, H. Li, J. Zhai, H. Yu, *In situ* growth of Prussian blue nanocrystal within Fe^{3+} crosslinking PAA resin for radiocesium highly efficient and rapid separation from water, Chem. Eng. J., 277 (2015) 40–47.
[46] Z. Du, M. Jia, X. Wang, Cesium removal from solution using PAN-based potassium nickel hexacyanoferrate(II) composite spheres, J. Radioanal. Nucl. Chem., 298 (2013) 167–177.
[47] W. Yinsong, L. Lingrong, W. Jian, Q. Zhang, Preparation and characterization of self-aggregated nanoparticles of cholesterol-modified O-carboxymethylchitosan conjugates, Carbohydr. Polym., 69 (2007) 597–606.
[48] H. Zhang, H. Zhong, L. Zhang, S. Chen, Y. Zhao, Y. Zhu, Synthesis and characterization of thermosensitive graft copolymer of N-isopropylacrylamide with biodegradable carboxymethylchitosan, Carbohydr. Polym., 77 (2009) 785–790.
[49] A. Nilchi, R. Saberi, M. Moradi, H. Azizpour, R. Zarghami, Adsorption of cesium on copper hexacyanoferrate–PAN composite ion exchanger from aqueous solution, Chem. Eng. J., 172 (2011) 572–580.
[50] G. Sheng, S. Yang, J. Sheng, D. Zhao, X. Wang, Influence of solution chemistry on the removal of Ni(II) from aqueous solution to titanate nanotubes, Chem. Eng. J., 168 (2011) 178–182.
[51] D.L. Guerra, R.R. Viana, C.J. Airoldi, Adsorption of thorium cation on modified clays MTTZ derivative, J. Hazard. Mater., 168 (2009) 1504–1511.
[52] W.A. Abbasi, M. Streat, Adsorption of uranium from aqueous solutions using activated carbon, Sep. Sci. Technol., 27 (1994) 1217–1230.
[53] M.M. Dubinin, L.V. Radushkevich, Equation of the characteristic curve of activated charcoal, Proc. Acad. Sci. Phys. Chem. Sect. USSR, 55 (1947) 331–333.
[54] H. Muhamad, H. Doan, A. Lohi, Batch and continuous fixed-bed column biosorption of Cd^{2+} and Cu^{2+}, Chem. Eng. J., 158 (2010) 369–377.
[55] T.S. Singh, K.K. Pant, Experimental and modelling studies on fixed bed adsorption of As(III) ions from aqueous solution, Sep. Purif. Technol., 48 (2006) 288–296.
[56] Z. Yu, T. Qi, J. Qu, Y. Guo, Application of mathematical models for ion-exchange removal of calcium ions from potassium chromate solutions by Amberlite IRC 748 resin in a continuous fixed bed column, Hydrometallurgy, 158 (2015) 165–171.
[57] C. Jeon, Removal of cesium ions from aqueous solutions using immobilized nickel hexacyanoferrate-sericite beads in the batch and continuous processes, J. Ind. Eng. Chem., 40 (2016) 93–98.
[58] A.F. Shaaban, A.A. Khalil, T.A. Lasheen, E.A. Nouh, Huda Ammar, polyamidoamine dendrimers modified silica gel for uranium(VI) removal from aqueous solution using batch and fixed-bed column methods, Desal. Water Treat., 102 (2018) 197–210.
[59] N. Yahaya, I. Abustan, M.F.P.M. Latiff, O.S. Bello, M.A. Ahmad, Fixed-bed column study for Cu(II) removal from aqueous solutions using rice husk based activated carbon, Int. J. Eng. Technol. IJET-IJENS, 11 (2011) 248–252.
[60] R. Han, D. Ding, Y. Xu, W. Zou, Y. Wang, Y. Li, L. Zou, Use of rice husk for the adsorption of Congo red from aqueous solution in column mode, Bioresour. Technol., 99 (2008) 2938–2946.
[61] R. Han, Y. Wang, X. Zhao, Y. Wang, F. Xie, J. Cheng, M. Tang, Adsorption of methylene blue by phoenix tree leaf powder in a fixed-bed column: experiments and prediction of breakthrough curves, Desalination, 245 (2009) 284–297.
[62] M. Calero, F. Hernainz, G. Blazquez, G. Tenorio, M.A.M. Lara, Study of Cr(III) biosorption in a fixed-bed column, J. Hazard. Mater., 171 (2009) 886–893.
[63] C.M. Futalan, C.C. Kan, M.L. Dalida, C. Pascua, M.W. Wan, Fixed-bed column studies on the removal of copper using chitosan immobilized on bentonite, Carbohydr. Polym., 83 (2011) 697–704.
[64] H.C. Thomas, Heterogeneous ion exchange in a flowing system, J. Am. Chem. Soc., 66 (1944) 1466–1664.
[65] Z. Aksu, F. Gonen, Biosorption of phenol by immobilized activated sludge in a continuous packed bed: prediction of breakthrough curves, Process Biochem., 39 (2004) 599–613.
[66] Y.H Yoon, J.H. Nelson, Application of gas adsorption kinetics. I. A theoretical model for respirator cartridge service time, Am. Ind. Hyg. Assoc. J., 45 (1984) 509–516.